



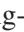



A High-Precision Modeling and Error Analysis Method for Mountainous and Canyon Areas Based on TLS and UAV Photogrammetry

Xiang-Long Luo , Nan Jiang , Hai-Bo Li , Huai-Xian Xiao , Xing-Zhen Chen , and Jia-Wen Zhou 

Abstract—Obtaining comprehensive and accurate terrain data is important for engineering construction. Unmanned aerial vehicle (UAV) photogrammetry and terrestrial laser scanning (TLS) are two widely used terrain modeling techniques. In mountainous areas, both techniques suffer limitations. These limitations occur in uninhabited areas, primarily caused by the steep terrain and inconvenient transportation conditions, resulting in poor data integrity and inadequate accuracy in UAV and TLS terrain mapping. In this article, we proposed a fusion modeling method based on UAV photogrammetry and TLS for high-precision terrain mapping in mountainous and canyon areas. The proposed method entails the use of TLS data to provide additional control points for UAV modeling, resulting in an improved accuracy of the modeling results. In addition, to quantify the optimization effect of this method, we proposed a 3-D model deviation comparison method based on the iterative closest point algorithm. This method can be employed to accurately depict the differences in distance and rotation angle between multiple terrain models. We applied this method to the Yebatan hydropower station in Southwest China, which increased the accuracy of the terrain data by 26% and expanded the effective range by over 100%.

Index Terms—Error analysis, terrain modeling, terrestrial laser scanning (TLS), unmanned aerial vehicle (UAV), Yebatan.

I. INTRODUCTION

HYDROPOWER stations are important livelihood projects that capture water flow to generate electricity in an environmentally friendly way [1], [2]. They also play a role in regulating water levels and flows, rendering them essential for energy supply and economic development purposes [3], [4]. In the design and construction process of hydropower stations, high-precision terrain data are particularly important [5], [6],

[7]. Designers must accurately understand terrain characteristics to estimate the amount of land grading, excavation, and filling required for construction, as well as the funding and resources needed for the project.

In contrast to general civil engineering projects, hydropower stations are usually built in uninhabited mountainous areas, as these areas typically exhibit steep terrain and abundant water sources, making them ideal locations for water storage [8], [9], [10]. In these mountainous areas, traditional manual measurement methods, such as total stations, suffer significant limitations. In these methods, discrete ground feature points are connected to create a terrain map with surface classification properties. In complex terrain environments, it is common to encounter sparse measurement points and a limited field of view, and it is difficult to obtain comprehensive terrain data. Moreover, manual measurement operations exhibit long working cycles and require a significant investment of manpower, resources, and finances, resulting in high costs. In addition, mountainous and canyon areas encompass steep terrain, dense vegetation, and extremely poor visibility conditions, posing significant safety risks for manual operations [11], [12], [13].

In recent years, remote sensing techniques, represented by terrestrial laser scanning (TLS), airborne light detection and ranging (LiDAR), and unmanned aerial vehicle (UAV) photogrammetry, have developed rapidly in the terrain measurement field [14], [15], [16], [17]. Compared with traditional methods, these technologies offer many advantages in terms of efficiency, data integrity, safety, and cost. With the use of TLS, surface point cloud data and highly accurate geometric spatial information can be obtained quickly [18], [19], [20]. The UAV platforms are highly flexible and capable of carrying a digital camera into the target area to acquire data with virtually no terrain constraints and no safety risks to the technician [21]. During UAV flight, the carried camera can take photos in both vertical and oblique directions. Some researchers have pointed out that, compared with the traditional method of acquiring photos only in the vertical direction, increasing the acquisition of photos in the oblique direction can improve the accuracy of the UAV modeling, especially in areas with steeper slopes [22]. At the same time, the position and orientation system (POS) of the UAV can record the position, direction, speed, etc., of the UAV during the flight. In a relatively short time, the UAV can complete the flight mission of the whole area and obtain the high-resolution

Manuscript received 3 September 2023; revised 4 December 2023 and 2 March 2024; accepted 23 March 2024. Date of publication 27 March 2024; date of current version 10 April 2024. This work was supported in part by the National Natural Science Foundation of China under Grant 52379105, Grant U2240221, and Grant 41977229 and in part by Sichuan Youth Science and Technology Innovation Research Team Project under Grant 2020JDTD0006. (Corresponding author: Jia-Wen Zhou.)

Xiang-Long Luo, Huai-Xian Xiao, and Xing-Zhen Chen are with the College of Water Resources and Hydropower, Sichuan University, Chengdu 610065, China (e-mail: 2022223060088@stu.scu.edu.cn; 2021223060094@stu.scu.edu.cn; 2021223060093@stu.scu.edu.cn).

Nan Jiang, Hai-Bo Li, and Jia-Wen Zhou are with the State Key Laboratory of Hydraulics and Mountain River Engineering, Sichuan University, Chengdu 610065, China (e-mail: 2018223060073@stu.scu.edu.cn; hbli@scu.edu.cn; jwzhou@scu.edu.cn).

Digital Object Identifier 10.1109/JSTARS.2024.3382092

image of a large area and the corresponding POS data. Then, through the image processing software, using the structure from motion algorithm reconstruction, the acquired large-scale overlapping images can be constructed into a complete point cloud of the target area [23], [24]. Due to the low cost, low time consumption, high applicability, and high data integrity of UAV photogrammetry, it has been widely used in risk assessment of various geological hazards [25], [26] and analysis of changes in regional topography [27], [28].

Airborne LiDAR and TLS are also widely used techniques in geotechnical engineering analysis. With reasonable flight plans, airborne LiDAR can acquire high-precision terrain data, which is commonly used in landslide susceptibility analysis, landslide mechanism analysis, and also used by many scholars for identifying different types of rock movements, rockfall susceptibility analysis [29], [30], [31]. Compared with TLS, airborne LiDAR has higher data integrity, but the operation and equipment cost of using airborne LiDAR is higher than TLS, and its accuracy is lower than TLS [29]. TLS needs to scan the target at a fixed scanning point on the ground, and it can provide 3-D spatial surface models with very high accuracy, which has been confirmed by some researchers' real measurements, and its measurement accuracy can reach the millimeter level. By acquiring scan data at different scan points and accurately stitching the scan data of each part, more complete terrain data can be obtained [32], [33]. Compared with airborne LiDAR, TLS has a lower cost and can provide more accurate data.

However, both TLS and UAV photogrammetry exhibit their own limitations in practical applications. For instance, in TLS, laser beams are emitted, and the reflection is then received to obtain spatial information from the target, which is an efficient and highly accurate approach [34], [35]. However, there are many blind spots and notable vegetation growth in areas, such as high mountains and canyons, where the scanner cannot collect sufficient data, resulting in limited completeness of the obtained point cloud. Zhou et al. [36] used TLS to explore mining subsidence areas. However, due to the limitations of the viewing angle, the scanning results showed significant data gaps [36]. Barbarella and Fiani [37] used TLS to monitor a large landslide. The obtained scan data showed favorable integrity in the lower part of the landslide, but only sparse data were available for the upper part [37]. Compared to TLS, in UAV photogrammetry, surface photos can be captured from multiple perspectives in the air, and this method achieves a significant advantage in data integrity, especially in mountainous and canyon areas [38], [39], [40]. However, there are accuracy issues with UAV photogrammetry. The modeling accuracy of UAV photogrammetry relies on the layout of ground control points (GCPs) [41], [42], [43]. In complex terrain, many positions are difficult to reach, making it difficult to manually set up GCPs. Without sufficient GCPs, the accuracy of UAV modeling is greatly reduced. For example, Lu and Yang [44] used the traditional method of establishing real-time kinematic (RTK) GCPs to conduct UAV modeling of landslide groups and debris flows in mountainous and canyon areas. The accuracy in areas without GCPs was poor, with a vertical error rate of 9.6% [44].

Until now, there have been many studies on the simultaneous use of multiple remote sensing techniques to acquire complex terrain data. Some researchers have used both UAV and TLS for monitoring landslide evolution, and in the process found that the TLS point cloud has higher accuracy, and the simultaneous use of the two technologies helps to improve the spatial coverage and density of the point cloud [33]. In some studies, UAV and airborne LiDAR were used to analyze the damage mechanisms and movement evolution of landslides, and it was found that UAVs have the advantage of being able to acquire DSM quickly and improve the data by supplementing it with photographs from lower flight altitudes, while airborne LiDAR has the advantage of being able to have higher accuracy [21]. There has also been research on the use of UAV imagery to supplement airborne LiDAR data for registration. When the accuracy of the airborne POS is low, the directly acquired airborne LiDAR data will have large distortions. The researcher proposed a method to correct and register airborne LiDAR data using UAV-oriented images, which resulted in a significant increase in the accuracy of the LiDAR point cloud data obtained when using a low-accuracy POS [45].

In most of the studies, different remote sensing techniques are used separately and the results are complemented or validated against each other, and the use of fusion between different techniques is still relatively rare.

The vertical error of the UAV model is the result of certain distortions during modeling. These distortions usually appear as rotations of local point clouds around a certain point or axis. To assess the accuracy of UAV modeling results, it is necessary to measure these distortions [46], [47]. However, it is difficult to measure the distortions of UAV modeling results because point clouds exhibit only spatial properties. It is difficult to obtain correspondences between two point clouds and accurately measure their differences [48]. Currently, commonly used methods for analyzing point cloud errors include shortest distance (SD), DEM of difference (DoD), and multiscale model-to-model cloud comparison (M3C2) [49]. Due to the respective applicability conditions and limitations of these methods, when they are applied to analyze the errors generated by UAV modeling, the calculation results at some points will have relatively large deviations from the actual values.

Based on the above, in this article, we proposed a new method for terrain modeling and error analysis based on TLS and UAV photogrammetry, mainly focusing on high-precision modeling in mountainous and canyon areas. In this method, a subset of prominent feature points is extracted from the TLS point cloud. Based on the high accuracy of TLS, these points are used as GCPs in the UAV modeling process, along with RTK GCPs. With enough GCPs, a highly accurate terrain model can be obtained. In terms of accuracy verification, we proposed an error quantification analysis method based on the iterative closest point (ICP) algorithm [50], [51], [52]. In this method, the target point cloud is divided into multiple blocks, and ICP registration is performed with the reference point cloud for each block, indirectly obtaining the centroid displacement error in each block based on the block centroid displacement in each

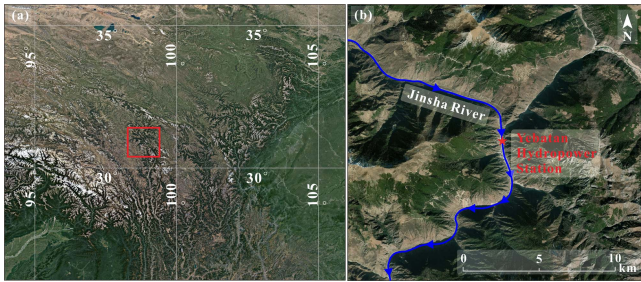


Fig. 1. Overview of the study area. (a) Satellite image of the Yebatan hydropower station. (b) Location map of the study area.

registration process. This error calculation method is based on precise point cloud matching and is highly applicable even under complex terrain conditions.

In this study, we conducted a modeling study of the Yebatan (YBT) hydropower station, Southwest China, which has steep terrain on both sides of the dam area and a relative height difference of more than 1000 m. Based on the proposed methods, we obtained a high-precision terrain model of the YBT Dam shoulder slope, which was verified by the error analysis method. The results showed that the accuracy of the modeling results obtained using the fusion modeling method is significantly improved relative to traditional modeling methods. This indicates that our method is effective and very important for high-precision terrain mapping in areas with complex terrain.

II. METHOD

A. Study Area

The YBT hydropower station is located upstream of the Jinsha River and is the 7th level in the 13-level development plan. The upstream station is the Bolo hydropower station, and the downstream station is the Lava hydropower station [53], [54]. The station is located in the lower reaches of the Jinsha River at the mouth of the Jiaogou River, which marks the border between Baiyu County, Sichuan Province, and Gongga County, Tibet (see Fig. 1).

The banks of the YBT hydropower station are characterized by robust and steep mountains, with mountain tops exceeding 4000 m in elevation and a relative height difference of over 1000 m, belonging to high mountain landforms. The valley is narrow with steep slopes, forming a symmetric deep V-shaped canyon (see Fig. 2). Under such conditions, it is extremely difficult to accurately obtain terrain data within this area. However, high-precision terrain data are crucial for the design and construction of hydropower plants. If low-precision terrain data were used in the design process, the construction plans and estimated project quantities would be uncertain, leading to numerous design changes during subsequent construction, which is detrimental to construction implementation and management. In the slope excavation project of the YBT Dam, a significant discrepancy was observed between the actual slope and the design slope, causing inconvenience in the construction process [see Fig. 2(b)]. Under terrain conditions such as those surrounding

TABLE I
UAV PARAMETER SETTINGS

UAV-FM-D2000	
Camera	Sony D-op3000
Altitude (aviation)	300 m
Flight mode	Fixed height
Average resolution	0.05 m
Overlap	>80%
Speed	10 m/s
Number of photos	1359
Application	UAVManager
Post-processing software	ContextCapture

the YBT hydropower station, traditional manual measurement methods are difficult to implement, time-consuming, and extremely dangerous. Therefore, a noncontact monitoring method is needed. In this study, both UAV photogrammetry and TLS were used for data collection on the slope of the YBT Dam, and the traditional UAV modeling method and the fusion modeling method were used to obtain a terrain model of the slope. The accuracy of these two models was quantitatively compared and analyzed using the error calculation method based on the ICP algorithm. The technical workflow is shown in Fig. 3.

B. Data Acquisition

UAV photogrammetry is a technique that uses UAVs equipped with tilt cameras to create a highly accurate terrain model of the ground surface. During the UAV flight, the tilt camera captures ground images from different angles. After these images are processed using specific algorithms, a terrain model of the ground surface can be obtained [23], [24].

The process of using UAV photogrammetry to create a terrain model of the ground surface can generally be divided into the following steps: parameters are determined such as the shooting area, flight altitude, and overlap degree and a flight plan is developed to ensure complete coverage of the area; the flight mission is executed to collect aerial image data while using the POS to record information, such as the position, speed, and altitude at the time of shooting; the collected image data are preprocessed, including image correction, dedistortion, color balance, and image stitching; ground feature points are extracted, photos are matched, aerial triangulation is performed based on POS information and GCPs information to determine the coordinates of each point on the ground; and the coordinate data obtained from aerial triangulation are processed to generate a terrain model of the ground surface.

UAV photogrammetry data were collected in this study using a Feima D2000 device, and the set flight parameters are listed in Table I.

The UAV route setting is shown in Fig. 4. We used a UAV with a five-lens camera to capture images in the vertical and four oblique directions during flight. After the UAV completed the flight mission, a total of 1359 photos were acquired, and UAV POS information was recorded. The brightness, clarity,

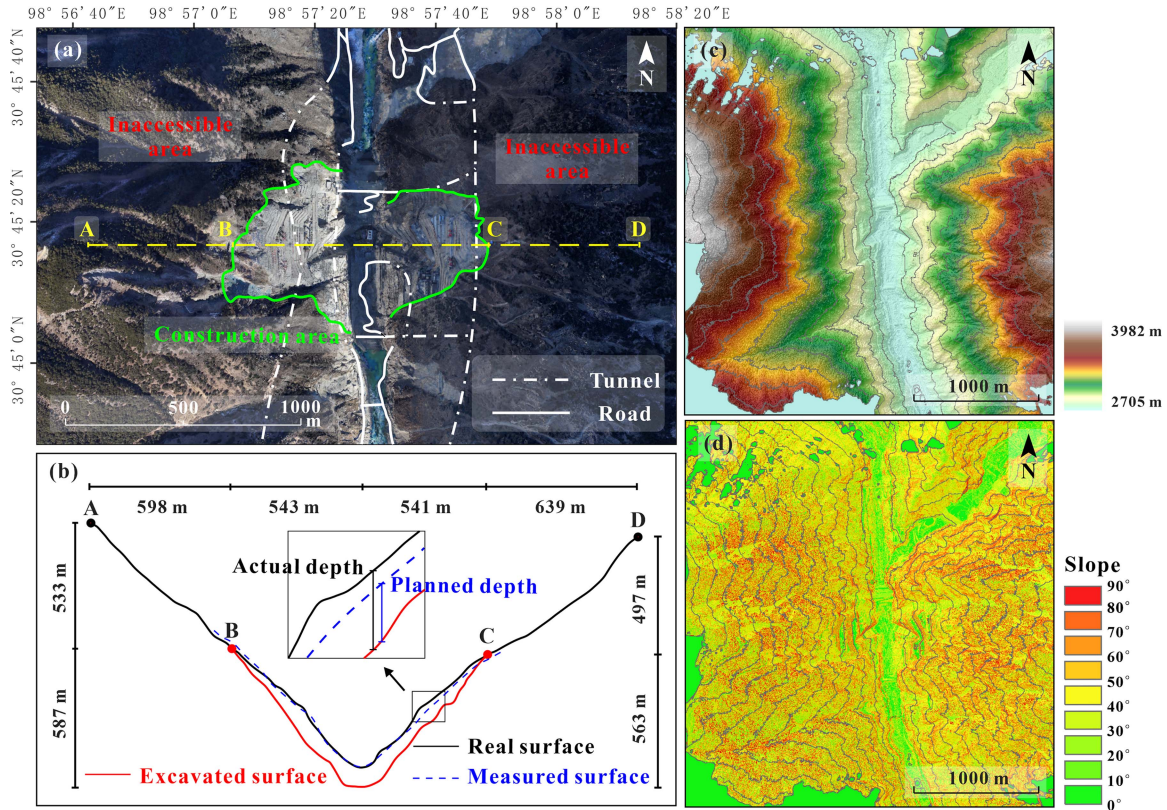


Fig. 2. Overview of the slopes on the shoulder of the Yebatan dam. (a) Road distribution and construction area based on UAV terrain modeling and field surveys. (b) Slope profile lines and real and surveyed surfaces. (c) Elevation maps. (d) Slope maps.

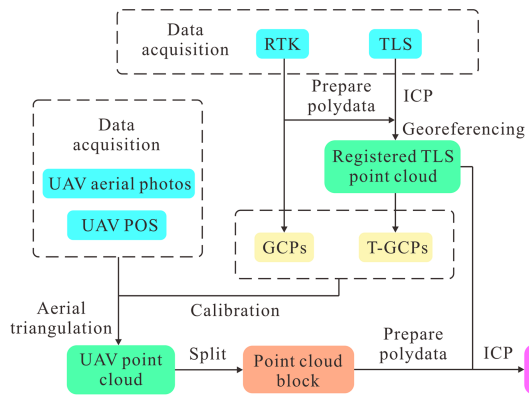


Fig. 3. Research workflow: Obtain RTK, TLS, and UAV data; acquire GCPs through RTK and TLS for providing geographic coordinates and correction in UAV modeling; segment the UAV point cloud and calculate the error using an error calculation method based on ICP registration.

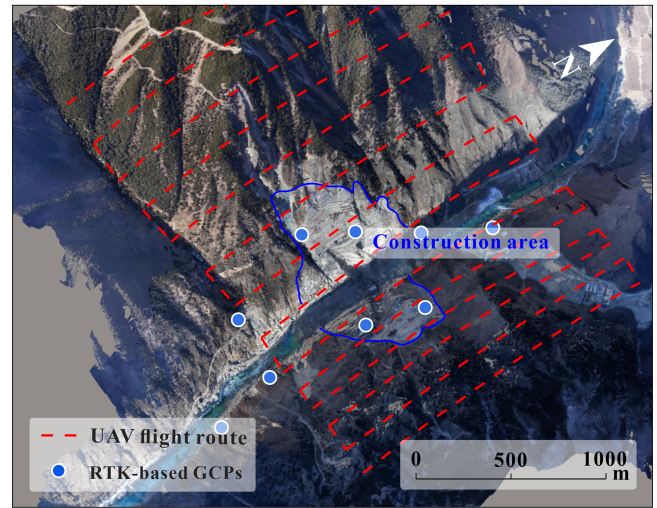


Fig. 4. UAV route setting and RTK GCPs placement.

and overlap of the acquired photos met the requirements, and they could be used for subsequent UAV modeling.

In addition, RTK GCPs must be set up to improve the accuracy of UAV modeling. In this study, a total of nine RTK GCPs were deployed along the river channel and the dam shoulder, and their precise geographic coordinates were obtained.

TLS is a high-precision technology for obtaining terrain point cloud data of the ground surface. It can be used to quickly obtain the coordinates, reflectivity, and texture information of a large number of points on the surface of the object being

measured, generating high-precision point cloud data. Compared to traditional single-point measurement methods, TLS provides many advantages. It can acquire a large amount of point cloud data in a short period of time, with the measurement accuracy reaching the millimeter level. In addition, it provides a high degree of automation in data processing. It is widely used in geological exploration, architecture, cultural heritage preservation, industrial design, and other fields [32], [33].

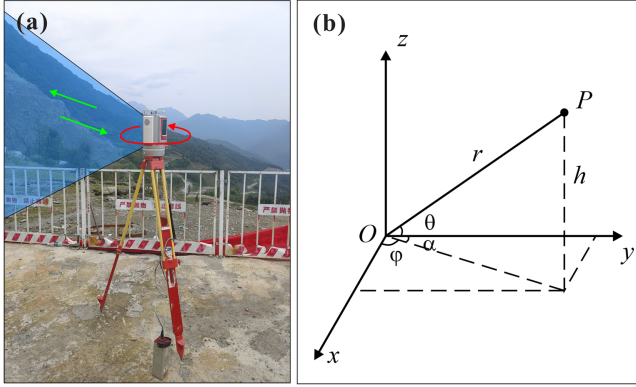


Fig. 5. TLS. (a) TLS working diagram. (b) Coordinate calculation.

TABLE II
TLS PARAMETER SETTINGS

Rigel VZ-2000i		
Scan mode	Panorama	
Angular resolution	Vertical	0.015°
	Horizontal	0.015°
Post-processing software	RiSCAN Pro	

In TLS, a laser is a beam emitted by a reflector or laser head to scan the surface of the target object. After the laser beam is reflected back, it is received by a receiver, and the time delay and optical path difference of the reflected beam are calculated to determine the distance r from the surface of the target object to the laser scanner (see Fig. 5). At the same time, by recording the horizontal angle φ and vertical angle θ of the scan, the three-dimensional spatial relative coordinate difference between each scan point and the station can be calculated [55], [56]. By continuously adjusting the scanning angle and direction of the scanner, a large amount of point cloud data for the surface of the object can be collected, resulting in a complete terrain point cloud.

The TLS point cloud coordinates can be calculated as follows:

$$\begin{aligned} x &= r \cos \varphi \cos \theta \\ y &= r \sin \varphi \cos \theta \\ z &= r \sin \theta \end{aligned} \quad (1)$$

where x , y , and z are the point cloud relative coordinates, r is the distance from the surface of the target object to the laser scanner, φ is the horizontal direction angle, and θ is the vertical direction angle.

In this study, a Rigel VZ-2000i terrestrial laser scanner was used to collect TLS data, which has millimeter accuracy. To improve the completeness of the scan data, a total of four scan positions were set up, two on the right dam shoulder and two on the left dam shoulder. The scanning parameters set are listed in Table II.

After scanning completion, we accurately registered each part of the point cloud using the ICP algorithm and obtained the TLS point cloud of the YBT Dam shoulder slope (see Fig. 6). The

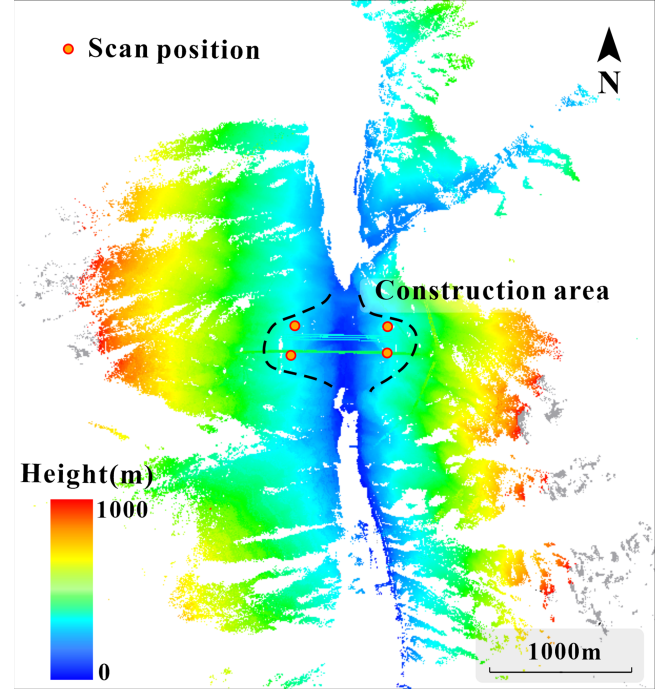


Fig. 6. TLS point cloud of the Yebatan Dam shoulder slope after accurate registration of the scan data from each site.

average density of the acquired TLS point cloud is about 150 points/m², and the denser places can reach 300 points/m².

C. Data Refinement Based on UAV Photogrammetry and TLS

The fusion of UAV and TLS data, in the conventional sense, refers to the combination of the two datasets through methods such as ICP algorithm registration, aiming to complement each other or improve the accuracy of data in certain areas [57], [58]. This data fusion method is more suitable for small-scale UAV modeling and TLS data because both exhibit a relatively high accuracy, enabling them to be combined quite well.

However, in this study, we focused on high-accuracy modeling in large-scale areas. The point cloud data from TLS can be considered accurate, while modeling using UAV data may suffer significant deviations, especially in areas far from GCPs. In this case, the traditional fusion of UAV and TLS data is not meaningful as the two cannot complement each other well. There are obvious layering phenomena and failure to achieve complementary effects when they are combined.

The data fusion method adopted in this study differs from the traditional fusion method. TLS point cloud data are used to assist in UAV modeling, and its core is to provide additional GCPs for the UAV modeling process.

In UAV photogrammetry modeling, the setup of GCPs is a very important task. The range, quantity, and accuracy of the setup of GCPs can significantly impact the modeling results using UAV aerial images. Therefore, in the process of using UAV photogrammetry for modeling, it is necessary to set up a sufficient number of GCPs with high accuracy to ensure the effectiveness of the UAV modeling results. Generally, GCPs are

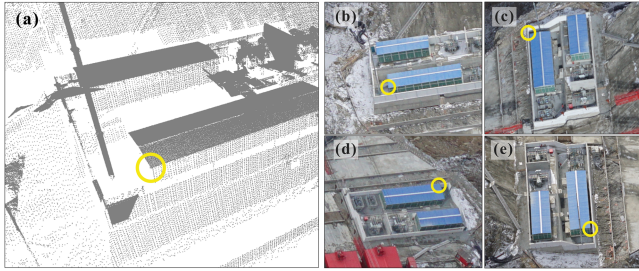


Fig. 7. Extract feature points from the TLS point cloud and calibrate them in UAV aerial photos. (a) Feature point in the TLS point cloud. (b), (c), (d) and (e) Feature points in UAV aerial photos.

obtained using RTK technology. However, in high mountain and canyon areas, due to the complex terrain, inaccessible roads, and significant safety hazards, a sufficient number of ground personnel cannot reach these areas, making it difficult to set up RTK GCPs. In the absence of sufficient RTK GCPs, using only a small number of GCPs for UAV modeling cannot guarantee the accuracy of the resulting terrain model.

TLS achieves high accuracy but its data completeness is far inferior to that of UAV photogrammetry when scanning in mountainous and canyon areas. This occurs because TLS relies on emitting lasers and receiving reflected information at points to complete data collection. In complex terrain, such as mountainous and canyon areas, there are numerous blind spots not reachable by lasers, resulting in missing data in the final scan result.

Based on the above characteristics, in this study, we proposed a TLS-UAV photogrammetry fusion modeling method. In the target monitoring area, the UAV is used to collect photogrammetry data, and RTK technology is employed to obtain GCPs at accessible locations. Simultaneously, TLS is used to scan the target area at multiple sites, and the point cloud data from each site are accurately registered using the ICP algorithm to obtain a complete TLS point cloud of the target area. At this point, the TLS point cloud data do not include coordinate information, so the known point coordinates obtained via RTK technology are imported into the TLS point cloud data to obtain the coordinates of each point in the point cloud data. Due to the millimeter-level accuracy of TLS, the obtained point cloud data coordinates can be considered sufficiently accurate. Prominent landmark points are selected from the TLS point cloud data as TLS GCPs. The position of the TLS GCPs is calibrated against UAV aerial photos, and their coordinates are input. This provides additional GCPs for UAV modeling (see Fig. 7), and a high-precision terrain model is then generated through aerial triangulation.

D. Accuracy Analysis Method for the 3-D Model

The commonly used methods for analyzing 3-D deformation errors are the SD method, DoD method, M3C2 method, etc.

In the SD method, the shortest distance from a point to the reference object is calculated as the error [see Fig. 8(a)]; in the DoD method, two-phase DEM data are compared, and the distance along the vertical direction from a computed point to the reference data is calculated as the error [see Fig. 8(b)] [49]. These two methods are relatively simple to use and suitable for

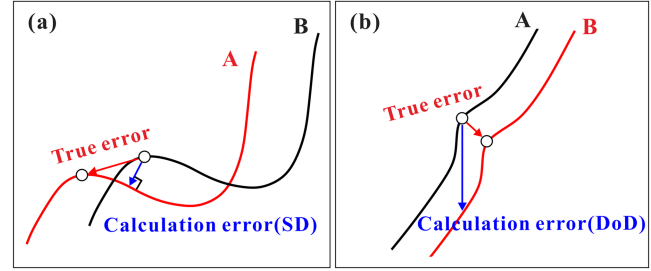


Fig. 8. True error and calculation error from different methods. (a) SD method. (b) DoD method.

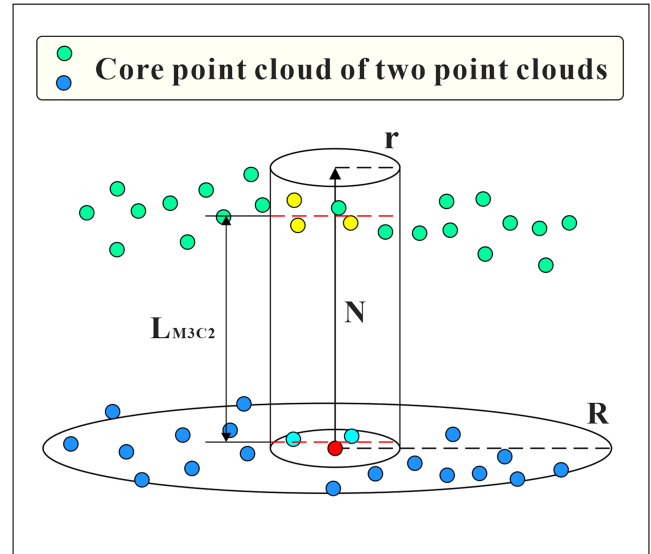


Fig. 9. M3C2 method.

point cloud error calculation in simple cases with low-accuracy requirements. However, both methods suffer severe limitations. In complex situations, these two methods can hardly find the correct corresponding points to calculate the error.

The M3C2 algorithm is a point cloud distance calculation method proposed by Lague et al. [49]. The algorithm starts by selecting the core point cloud. At a given core point, it fits the surrounding point cloud data within a specified radius R to form a plane and constructs a cylinder along the normal direction of the plane with a radius of r . The average positions of the original point cloud and the reference point cloud within the cylinder are calculated separately, and the distance between the average positions is used as the distance of the core point relative to the reference point cloud (see Fig. 9). The M3C2 algorithm is well suited to a point cloud that changes along the normal direction with respect to the reference point cloud. However, if there is significant misalignment between the two point clouds along the direction perpendicular to the normal, the algorithm may produce large deviations in the calculation results. In complex and varied terrain point cloud models obtained in mountainous canyon areas, none of the abovementioned error calculation methods can achieve satisfactory results for error analysis.

In this study, we proposed an error analysis method based on the ICP algorithm. Compared to traditional error analysis

methods, this method is based on point cloud matching, which can be employed to accurately identify corresponding point pairs between different point clouds. It achieves higher adaptability and accuracy.

The ICP algorithm is a classical point cloud registration method. It aims to estimate a rigid transformation matrix by minimizing the error between the matching point cloud and the reference point cloud. The rigid transformation matrix is continuously optimized through iteration until the convergence condition is met. The point cloud P can be matched to the reference point cloud Q by a spatial rotation matrix M and a spatial translation vector \vec{t}

$$Q = MP + \vec{t} \quad (2)$$

$$M = \begin{bmatrix} r_{11} & r_{12} & r_{13} \\ r_{21} & r_{22} & r_{23} \\ r_{31} & r_{32} & r_{33} \end{bmatrix}, \vec{t} = \begin{bmatrix} t_x \\ t_y \\ t_z \end{bmatrix}. \quad (3)$$

Each iteration of the computational process can yield a spatial rotation matrix M_n and a spatial translation vector \vec{t}_n . To obtain the total transformation matrix of the point cloud P in the matching process, M_n and \vec{t}_n are converted into 4×4 matrices R_n and T_n as follows:

$$T_n = \begin{bmatrix} 1 & 0 & 0 & t_x^n \\ 0 & 1 & 0 & t_y^n \\ 0 & 0 & 1 & t_z^n \\ 0 & 0 & 0 & 1 \end{bmatrix}, R_n = \begin{bmatrix} r_{11}^n & r_{12}^n & r_{13}^n & 0 \\ r_{21}^n & r_{22}^n & r_{23}^n & 0 \\ r_{31}^n & r_{32}^n & r_{33}^n & 0 \\ 0 & 0 & 0 & 1 \end{bmatrix}. \quad (4)$$

The transformation of each iteration of p_i in P can be rewritten as

$$\begin{aligned} p_i^n &= T_n \times R_n \times p_i^{n-1} \\ &= \begin{bmatrix} r_{11}^n & r_{12}^n & r_{13}^n & t_x^n \\ r_{21}^n & r_{22}^n & r_{23}^n & t_y^n \\ r_{31}^n & r_{32}^n & r_{33}^n & t_z^n \\ 0 & 0 & 0 & 1 \end{bmatrix} \times \begin{bmatrix} x_{p_i^{n-1}} \\ y_{p_i^{n-1}} \\ z_{p_i^{n-1}} \\ 1 \end{bmatrix} = \begin{bmatrix} x_{p_i^n} \\ y_{p_i^n} \\ z_{p_i^n} \\ 1 \end{bmatrix}. \end{aligned} \quad (5)$$

Then, the spatial rotation matrix and spatial translation vector in each iteration can be combined into the same spatial transformation matrix

$$M_{RT}^n = \begin{bmatrix} r_{11}^n & r_{12}^n & r_{13}^n & t_x^n \\ r_{21}^n & r_{22}^n & r_{23}^n & t_y^n \\ r_{31}^n & r_{32}^n & r_{33}^n & t_z^n \\ 0 & 0 & 0 & 1 \end{bmatrix}. \quad (6)$$

By multiplying the obtained M_{RT}^n in each iteration, the desired spatial transformation matrix M_{RT} for transforming point cloud P to P^n can be obtained

$$M_{RT} = \sum_{i=1}^n M_{RT}^i. \quad (7)$$

However, the ICP algorithm cannot be directly used for error analysis. First, using the ICP algorithm to register the matching point cloud with the reference point cloud alters the overall position of the matching point cloud, but it does not affect the shape of the point cloud in the registration process. When there

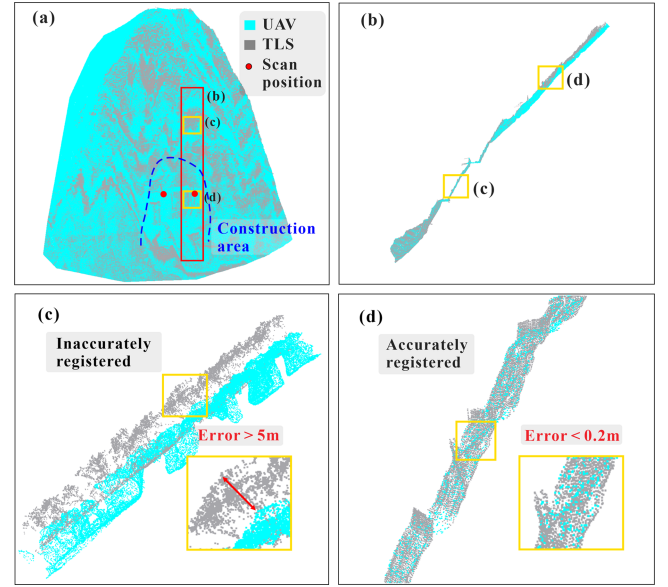


Fig. 10. Local layering phenomena in ICP registration. (a) Registered UAV point cloud and TLS point cloud. (b) Profile along the slope. (c) Clearly layered upper part of the profile. (d) Accurately registered lower part of the profile.

are shape differences between the matching point cloud and the reference point cloud, it is not possible to individually register each part of the point cloud. Therefore, the final registration result is only an overall optimal solution, and precise registration of each local part cannot be achieved. In some parts, there may be layering phenomena between the matching point cloud and the reference point cloud. Therefore, it is not possible to obtain error analysis results for inaccurately registered parts through the transformation matrix (see Fig. 10).

Moreover, the core of using point cloud registration for error analysis is obtaining a transformation matrix after ICP registration, which allows us to determine the translation and rotation magnitudes in the alignment process of the matching point cloud to the reference point cloud. However, in the matrix transformation method of the ICP algorithm, the coordinate origin is adopted as the rotation center of the matching point cloud. When the coordinate origin is not at the centroid of the point cloud block, the rotation matrix can cause displacement of the centroid of the point cloud. If the coordinate origin is far from the centroid of the point cloud block, even a small rotation can cause significant displacement of the centroid. This can make the iteration process of the ICP algorithm difficult and lead to less accurate registration results. Furthermore, in the obtained transformation matrix, the translation vector does not equal the true displacement of the centroid of the point cloud block. Further calculations are needed to obtain the true displacement of the centroid. Therefore, it is not advisable to use the original coordinate origin for ICP registration in error analysis.

In this study, we proposed an error analysis method based on the ICP algorithm.

First, the point cloud must be divided into blocks [see Fig. 11(c)] to perform ICP registration between each block and the reference point cloud, achieving accurate matching between

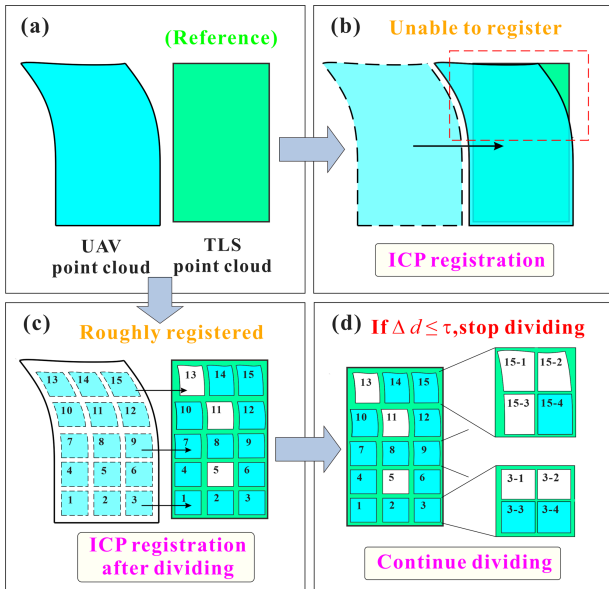


Fig. 11. Point cloud division and registration process. (a) UAV point cloud and TLS point cloud used as reference. (b) Direct registration using the entire point cloud. (c) Individual registration of each block after division. (d) Further division of each block and continued registration (the white blocks indicate that the threshold τ is reached and no further division is performed).

local point clouds and the reference point cloud and analyzing the error of each part of the matched point cloud.

In the block division process, multiple block divisions are adopted. The block size of the point cloud should not be too large as a large block size may result in the failure to register some areas, affecting the accuracy of error analysis. Conversely, it is also not advisable to divide the point cloud into excessively small blocks at once because when the point cloud blocks are far from the reference point cloud, excessively small blocks may cause the ICP algorithm to fail to correctly match the point cloud blocks with the reference point cloud. Therefore, multiple block divisions are used to gradually reduce the size of the point cloud blocks. After each division, ICP registration is performed to obtain a spatial transformation matrix. In this process, each point cloud block is gradually matched to the reference point cloud.

A threshold value τ is set, and the displacement value of the point cloud block in each registration process is denoted as Δd . When $\Delta d \leq \tau$, the point cloud block and the reference point cloud are considered to be fully aligned [see Fig. 11(d)]. At this point, the displacements of the centroids of the point clouds in each registration process are superimposed to obtain the total displacement of the centroid in the registration process.

Furthermore, when using the ICP algorithm to register point cloud blocks, the centroid of the point cloud block is used as the coordinate origin. In this case, the rotation center of the point cloud block is the centroid of the point cloud block, and the rotation and translation processes are independent, which is beneficial for the ICP algorithm to obtain accurate results. Moreover, after obtaining the transformation matrix via the ICP registration process, the translation directly obtained from this transformation matrix is the accurate displacement value of the centroid in the registration process.

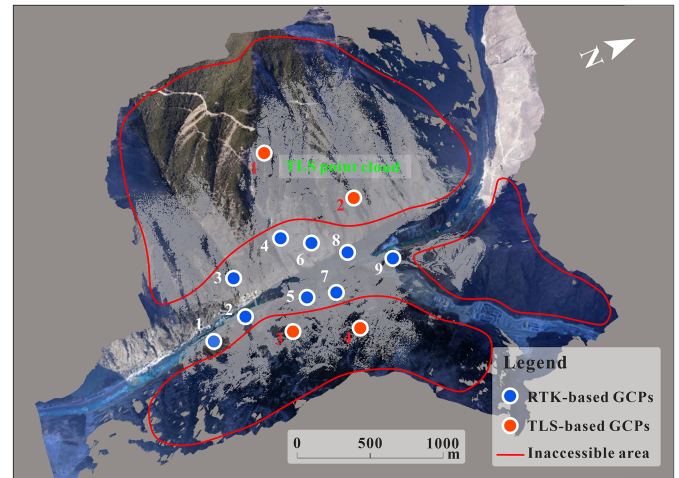


Fig. 12. Layout of the GCPs (RTK GCPs and TLS GCPs).

III. RESULTS

A. Modeling Data Acquisition

The setup of GCPs plays an important role in UAV modeling. If conditions allow, as many GCPs as possible should be established. In our data collection, a total of nine GCPs were obtained through RTK. Due to terrain restrictions and inaccessible roads, the RTK GCPs were mainly located along the river channel with some GCPs placed on the dam shoulder.

The coordinates of the GCPs obtained from RTK were imported into the TLS point cloud data of the YBT Dam shoulder high slope for point cloud georeferencing, thus obtaining the coordinates of all points in the point cloud. The obtained TLS point cloud is also considered as a true terrain reference for analyzing the accuracy of the UAV modeling results. When selecting GCPs from the TLS point cloud, select areas lacking RTK GCPs. The distance between the different GCPs is about 300–400 m. Finally, four points with obvious features were selected as TLS GCPs. The layout of the RTK GCPs and TLS GCPs is shown in Fig. 12.

We used ContextCapture software to process the UAV data, with control points imported from RTK GCPs and TLS GCPs, connection point density set to high, point cloud output format set to LAS, and point cloud sampling distance set to 2 pixels.

Based on the RTK GCPs information, the traditional method was used for UAV modeling, and the obtained terrain model was used as the control group for subsequent comparative analysis of the model accuracy.

Then the RTK GCPs and TLS GCPs were used together as GCPs for UAV modeling. Modeling results were obtained for the experimental group of this study. The UAV modeling point cloud densities obtained by each of the above two methods are approximately 100 points/m².

B. Block Error Calculation

After obtaining modeling results using the above two methods, accuracy verification and comparative analysis were

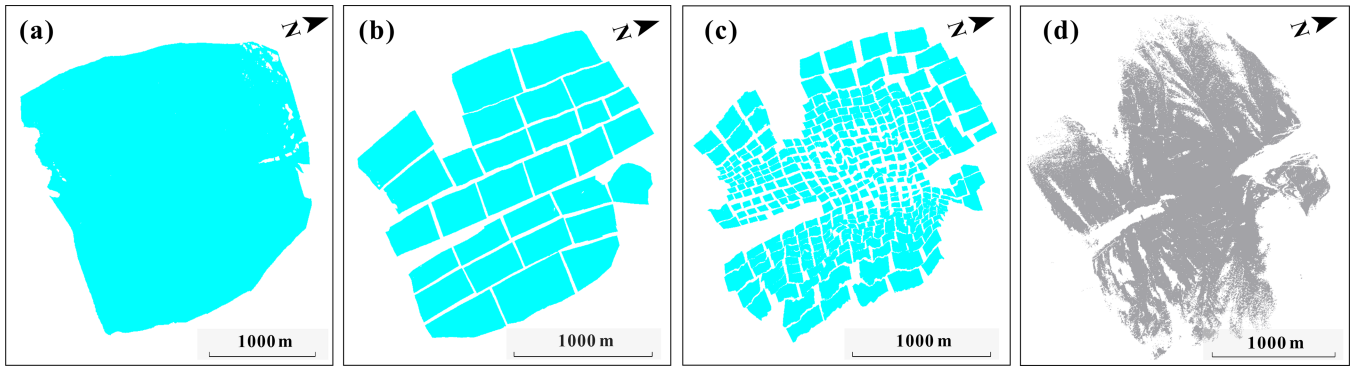


Fig. 13. Process of dividing the UAV point cloud. (a) Original UAV point cloud. (b) Result after the initial division of the UAV point cloud. (c) Result after multiple divisions of the UAV point cloud. (d) TLS point cloud.

conducted. As mentioned earlier, we used the error analysis method based on the ICP algorithm. In this study, since the TLS point cloud data exhibit relatively high accuracy, we used them as the standard reference.

The point cloud data obtained by UAV modeling were divided into blocks multiple times [see Fig. 13(a)–(c)]. After each division, the point cloud blocks were registered with the TLS point cloud using ICP.

We used a step-by-step approach in the point cloud division. To obtain a more detailed error distribution, we need to obtain the error of a sufficiently large number of points. However, if the point cloud is divided too small directly, the point cloud may not be correctly registered. By gradually dividing the point cloud and performing multiple alignments, the target points can be gradually aligned to the correct location to avoid incorrect registration or nonregistration. In the first division, we divide the point cloud into blocks of a few hundred meters by a few hundred meters, and after performing one registration, this larger block is further divided into two–four blocks for the next registration. In the registration process, the block centroid is used as the coordinate origin to ensure that the rotation center of the obtained transformation matrix is the point cloud centroid. The threshold is defined as $\tau = 0.1$ m. When the movement distance Δd of the block centroid in one ICP registration process is not greater than τ , it is considered that the point cloud block has been accurately registered with the TLS point cloud.

However, during the registration process, we did not make all the blocks meet the threshold. We met the threshold in the part of the center of the UAV point cloud where the accuracy is high enough. The error of these regions is only about 0.1 m, which allows them to meet the threshold after several divisions. For the regions with large errors, on the one hand, it is not useful to calculate the error too precisely because the error value itself is large, and at the same time, it is difficult to meet the threshold because of the large variation of the error in these regions. Therefore, in these regions, we performed appropriate division but did not make them meet the threshold. In addition, in a small number of regions where the TLS point cloud is missing, the point cloud block could not be correctly registered, so the blocks in these parts were discarded. In our computational process, regions with high accuracy stop dividing

after meeting the threshold. The regions with higher errors do not need to meet the threshold and stop dividing after a reasonable number of divisions. Based on the transformation matrices obtained from multiple ICP registration processes, the displacement of the point cloud block from the initial position to the registered position is calculated. To compare and analyze the errors between the control group and the experimental group, the same block division method is applied to the UAV point cloud of the control group and the experimental group to avoid the influence of different block division methods on the error comparison results.

C. Accuracy Analysis of the 3-D Model

This study primarily focuses on the horizontal and vertical errors of UAV point clouds. Therefore, based on the calculated displacements of the point cloud block centroids, the displacements along the x and y directions are combined to obtain the horizontal displacement, while the displacement along the z direction represents the vertical displacement. In this way, the horizontal and vertical errors of each point cloud block centroid with respect to the TLS point cloud can be obtained. Based on the position of the centroid of the point cloud blocks and the calculated error value and using the inverse distance weighting method for differencing, error distribution maps of the UAV modeling results obtained using the different methods are generated, as shown in Figs. 14 and 15.

The nine RTK GCPs are mainly distributed along the river and the shoulders of the dam. Based on the error distribution maps, the UAV modeling result obtained by the traditional method generally exhibits smaller errors in the direction along the river and near the dam shoulders. The horizontal and vertical errors of the centroid of the point cloud blocks in these areas are all within 0.5 m. However, as we move up along the slopes on both sides of the river and further away from the GCPs area, the horizontal and vertical errors of the centroid of the point cloud blocks begin to increase significantly. The horizontal and vertical errors in these areas are generally above 0.5 m. At the edge of the model, the horizontal and vertical errors of the centroid of the point cloud blocks reach more than 8 m.

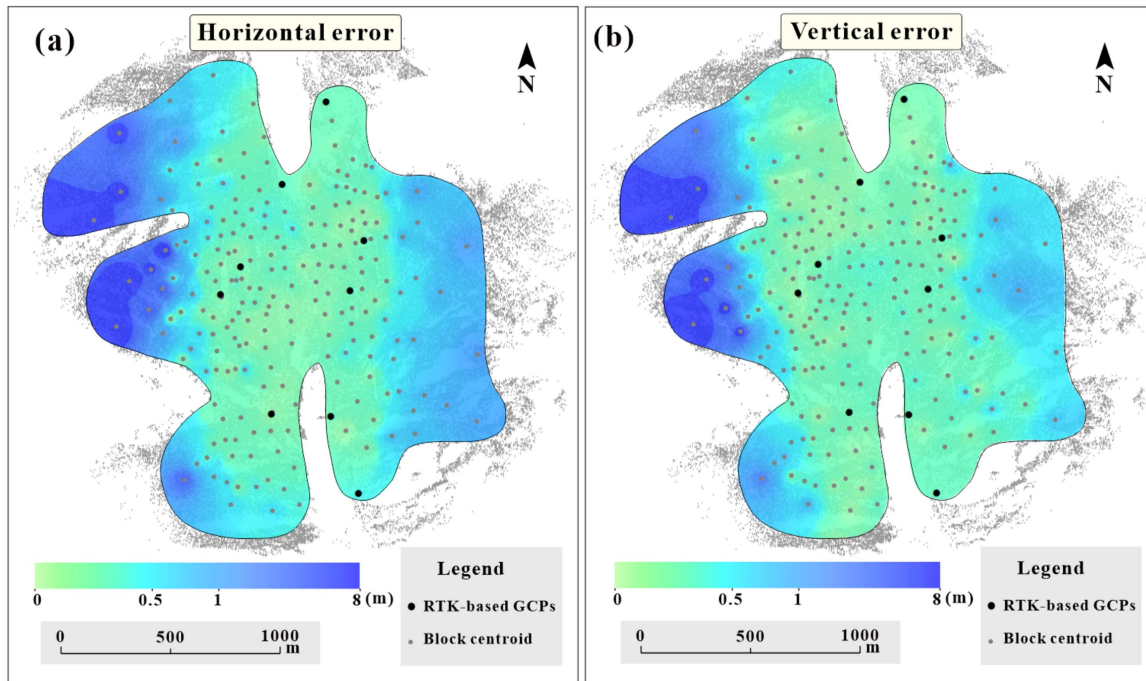


Fig. 14. Errors in the modeling results of the traditional method. (a) Horizontal errors. (b) Vertical errors.

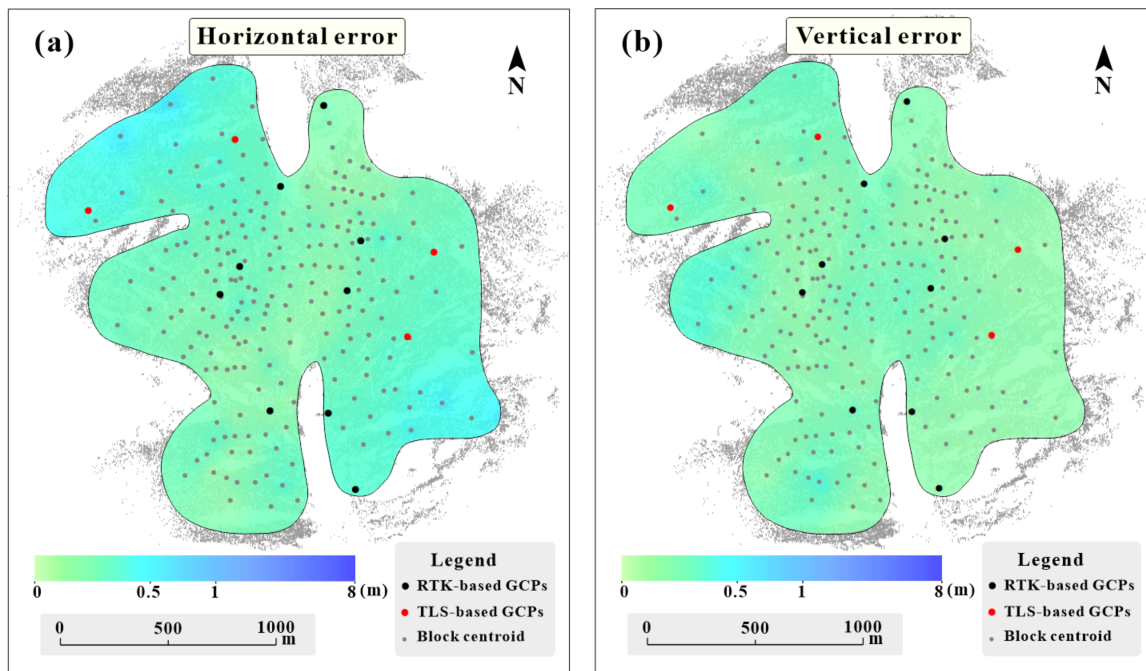


Fig. 15. Errors in the modeling results of the fusion method. (a) Horizontal errors. (b) Vertical errors.

The GCPs used in the fusion method include nine RTK GCPs and four TLS GCPs. The four TLS GCPs are distributed on the higher slopes on both sides of the river. According to the error distribution maps, near the areas of the nine RTK GCPs, the errors of the UAV modeling result obtained by the fusion method are not significantly different from those of the UAV modeling result obtained by the traditional method. Both the

horizontal and vertical errors are within 0.5 m. However, in the higher slope areas on both sides, the errors of the UAV modeling result obtained by the fusion method are significantly smaller. In these areas, the horizontal and vertical errors of most point cloud centroids are still within 0.5 m. At the edge of the model, some individual point cloud centroids exhibit horizontal errors above 0.5 m but all are within 0.6 m.

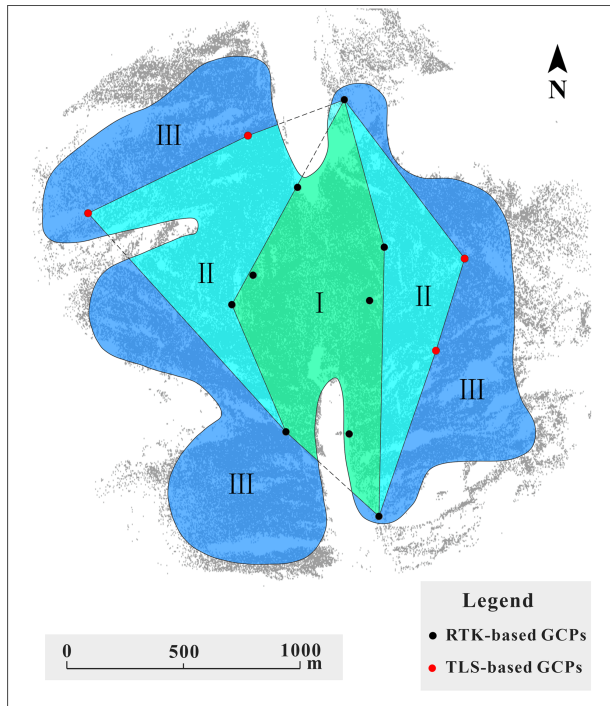


Fig. 16. Result of area division: Class I region, enclosed by the RTK GCPs; Class II region, enclosed by the RTK GCPs and TLS GCPs; and Class III region, outside the area enclosed by the RTK GCPs and TLS GCPs.

Based on the positions of the RTK GCPs and TLS GCPs, the error distribution map can be divided into three categories: Class I region, enclosed by the RTK GCPs; Class II region, enclosed by the RTK GCPs and TLS GCPs; and Class III region, outside the area enclosed by the RTK GCPs and TLS GCPs, as shown in Fig. 16.

The average horizontal error, maximum horizontal error, average vertical error, and maximum vertical error of the point cloud block centroids in the three types of regions are calculated, and the statistical results are provided in Table III.

The table reveals that in the Class I area, the average and maximum errors of the modeling results obtained using both the traditional method and the fusion method are relatively small, with the modeling result of the fusion method yielding slightly smaller errors. However, in the Class II and Class III areas, the average and maximum errors of the modeling result obtained using the traditional method significantly increased. In the Class III area, the average horizontal error of the modeling result of the traditional method is 1.12 m, and the average vertical error is 0.95 m. Moreover, both the maximum horizontal and vertical errors exceed 8 m. The errors of the modeling result of the fusion method do not show a significant increase in the Class II and Class III areas, with slightly larger average errors in the Class II area than in the Class I area and slightly larger average errors in the Class III area than in the Class II area. In the Class III area, the maximum horizontal error of the modeling result of the fusion method is only 0.59 m. This indicates that the TLS GCPs outside the range of the RTK GCPs play a significant role in the accuracy of the model. Based on the error analysis results, we can conclude that the fusion method improves the

TABLE III
ERROR STATISTICS RESULTS FOR THE THREE TYPES OF REGIONS

Errors (m)		
Class I region	Traditional	Fusion
Avg. (horizontal)	0.18	0.15
Max. (horizontal)	0.47	0.37
Avg. (vertical)	0.20	0.13
Max. (vertical)	0.36	0.25
Class II region	Traditional	Fusion
Avg. (horizontal)	0.73	0.23
Max. (horizontal)	7.48	0.49
Avg. (vertical)	0.50	0.13
Max. (vertical)	7.88	0.32
Class III region	Traditional	Fusion
Avg. (horizontal)	1.12	0.25
Max. (horizontal)	8.62	0.59
Avg. (vertical)	0.95	0.14
Max. (vertical)	8.19	0.45

terrain accuracy by 26% and increases the effective range by over 100%. This method has positive significance for terrain mapping in mountainous and canyon areas.

IV. DISCUSSION

High-precision modeling in high mountain and canyon areas is a difficult problem. Its main characteristics include high and steep terrain, large undulations, inconvenient transportation, and high danger. The aim of our study is to combine the advantages of TLS and UAV in order to obtain high-precision modeling data in these areas.

In previous studies, when both UAV and TLS techniques were used, the data obtained from the UAV and the TLS were analyzed separately and then the results were complemented or validated against each other [25], [33], which did not improve the shortcomings of the respective data. In our study, we attempted to combine the high accuracy of TLS with the high integrity of UAV to obtain higher quality modeling results.

The key of our method is that we extracted some of the marker points with high accuracy from the TLS data as a supplement to the GCPs for UAV modeling. In the absence of sufficient RTK GCPs, the addition of TCP GCPs can greatly improve the accuracy of the UAV modeling so that we can obtain the modeling results with high accuracy and high completeness.

In high mountain and canyon areas where it is difficult to set up enough RTK GCPs, the fusion method can greatly improve the accuracy of UAV modeling results. In the precision analysis results, the modeling results using the fusion method have higher accuracy in different areas, especially in the areas farther away from the RTK GCPs. We selected two small areas for the comparison of the point clouds obtained by different methods (see Fig. 17), in which the TLS point cloud is considered as the standard reference. In the two selected areas, the errors of the point cloud obtained by the traditional method are more than

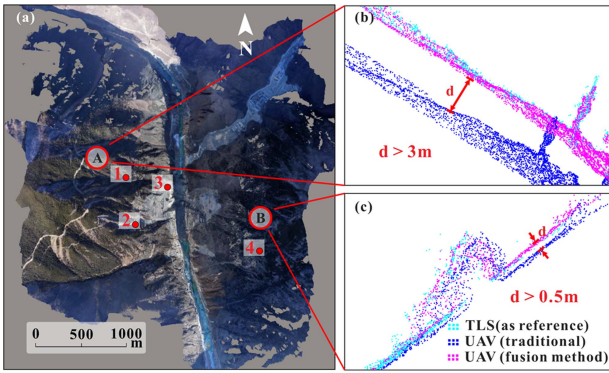


Fig. 17. Comparison of point clouds obtained by different methods. (a) Location of the comparison area. (b) Comparison results for region A. (c) Comparison results for region B.

TABLE IV
ERROR CALCULATION RESULTS OF THE DIFFERENT METHODS

Errors (m)					
Point	SD	DoD	M3C2	ICP	Actual
1	1.78	2.37	1.91	1.85	1.83
2	0.16	0.23	0.18	0.20	0.20
3	0.16	0.19	0.17	0.17	0.17
4	0.52	0.74	0.58	0.65	0.67

3 m and more than 0.5 m, while the point clouds obtained by the fusion method are well matched with the TLS point clouds.

In order to precisely quantify the accuracy of the obtained model, we propose a point cloud error analysis method based on the ICP algorithm.

We divided the UAV point cloud into blocks and registered it with the TLS point cloud. After multiple divisions and registration, we can get the transformation matrix for each block in the process of registration. Furthermore, the error values at different points can be obtained by calculation.

In past studies, the comparison between point clouds was often performed by algorithms, such as SD, DoD, and M3C2 [49]. In order to compare the accuracy of these methods with our method, we selected four measurement points from the UAV model obtained through the traditional method and calculated their errors using different methods. The positions of the measurement points are shown in Fig. 17(a). The actual errors were manually computed as a reference, and the results are listed in Table IV. The table indicates that the results obtained by the error calculation method based on the ICP algorithm are very close to the actual errors at the different measurement points, and in general, its accuracy is better than that of the other methods.

At the same time, our study has some shortcomings.

Finding suitable marker points from the TLS point cloud to be used as TLS GCPs is not an easy task, which depends on whether there are points with distinctive features and fixed locations in the TLS point cloud, and the locations of these points should also be distributed. In this study, we obtained a total of four TLS GCPs from the TLS point cloud. In fact, it would be better if more TLS GCPs could be obtained in regions where there

are still no GCPs. However, the results show that even with the inclusion of only four TLS GCPs, the accuracy of the modeling results obtained is greatly improved.

Missing or insufficient density in certain regions of the TLS point cloud can affect error analysis. During the error analysis in this study, a transformation matrix was obtained by aligning the point cloud blocks with the TLS point cloud. However, the TLS point cloud provides a limited coverage range and does not achieve complete coverage of the UAV point cloud. The effective coverage of the TLS point cloud is approximately 70% of the UAV modeling results. Therefore, a complete error analysis of the UAV point cloud cannot be performed. In addition, due to missing data in the partial blind zone and sparse point cloud at the edges of the TLS point cloud, it is difficult to obtain correct results by the ICP algorithm in these areas. As a result, a portion of the point cloud blocks were discarded in the actual error calculation process. Error calculations were only performed in areas where both the UAV point cloud block and the corresponding TLS point cloud were relatively complete. This had some impact on the accuracy of the error analysis.

When calculating the error of the UAV modeling results, the regions with large errors were not consistently divided into blocks to meet the threshold requirement. This is because of the fact that in regions with large errors, it is not necessary to calculate the errors too precisely due to the large error values themselves. Moreover, due to the large variation of error values in these regions, it is very difficult to make them meet the threshold requirement. Therefore, we performed appropriate segmentation in these regions but did not make them reach the threshold.

In this study, manual segmentation was employed to divide the UAV point cloud. However, this approach introduces subjective factors that can affect the accuracy of subsequent error analysis. In future work, the use of artificial intelligence algorithms for segmenting the UAV point cloud can be considered, which can optimize the process of point cloud division, eliminate subjective human factors, and drive the calculation error closer to the actual value.

It should also be noted that the error analysis method proposed in this study can not only be used for error analysis of terrain modeling results but can also be applied to a wide range of point cloud deformation analysis calculations. For example, based on the two-phase point cloud data of a landslide, after accurately registering the undeformed area, multiple block divisions of the point cloud data of one phase of the landslide can be performed. By conducting ICP registration of the other phase of the landslide point cloud data, accurate landslide deformation analysis can be achieved. By incorporating artificial intelligence algorithms for point cloud automatic segmentation, it can be possible to automate and accurately calculate large-scale point cloud deformation.

V. CONCLUSION

In this article, we propose a high-precision modeling method for mountainous and canyon areas. The method can significantly improve the accuracy of UAV modeling in areas where it is not

possible to place enough GCPs. Using this method, we modeled the YBT Dam shoulder high slope. The terrain model created using this method exhibits a significantly higher accuracy than that created using the traditional method, with the maximum error reduced from over 8 m to within 0.6 m. The fusion method improves the terrain accuracy by 26% and increases the effective range by over 100%.

To verify the accuracy of the UAV modeling results, we propose an error analysis method based on the ICP algorithm. This method gradually refines the error of the point cloud through blocking and ICP registration. Compared with several commonly used point cloud discrepancy calculation methods, this method has better accuracy in this study. Using this method, an error analysis of the terrain modeling results of the YBT Dam shoulder slope was conducted, and a horizontal error distribution map and vertical error distribution map were obtained. The error analysis results showed that the terrain modeling results obtained by the fusion method have a significantly higher accuracy than the results obtained by the traditional method.

REFERENCES

- [1] L. Xiao, J. Wang, B. Wang, and H. Jiang, "China's hydropower resources and development," *Sustainability*, vol. 15, no. 5, Mar. 2023, Art. no. 3940, doi: [10.3390/su15053940](https://doi.org/10.3390/su15053940).
- [2] Y. Tian, X. Lei, Q. Yu, and J. Sun, "Research on power benefits assessment of SiPing hydropower station under the operation of Sanliping hydropower station," *Int. Conf. Appl. Phys. Ind. Eng.*, vol. 24, pp. 512–517, Mar. 2012, doi: [10.1016/j.phpro.2012.02.074](https://doi.org/10.1016/j.phpro.2012.02.074).
- [3] Y. Li, J. Chang, and X. Li, "Small hydropower station monitoring system structure analysis," in *Proc. Int. Conf. Elect. Control Eng.*, 2010, pp. 1965–1967, doi: [10.1109/ICECE.2010.483](https://doi.org/10.1109/ICECE.2010.483).
- [4] H. Ye, J. Huang, J. Li, and Z. Zhou, "Short term output prediction method of runoff type medium and small hydropower stations," in *Proc. 4th Int. Conf. Elect. Eng. Control Technol.*, 2022, pp. 407–413, doi: [10.1109/ceect55960.2022.10030281](https://doi.org/10.1109/ceect55960.2022.10030281).
- [5] Y. Yang et al., "Characteristics analysis of the reservoir landslides base on unmanned aerial vehicle (UAV) scanning technology at the Maoergai Hydropower station, Southwest China," in *Proc. IOP Conf. Ser., Earth Environ. Sci.*, 2019, vol. 349, Art. no. 012009, doi: [10.1088/1755-1315/349/1/012009](https://doi.org/10.1088/1755-1315/349/1/012009).
- [6] M. Glendell et al., "Testing the utility of structure-from-motion photogrammetry reconstructions using small unmanned aerial vehicles and ground photography to estimate the extent of upland soil erosion," *Earth Surf. Processes Landforms*, vol. 42, no. 12, pp. 1860–1871, Sep. 2017, doi: [10.1002/esp.4142](https://doi.org/10.1002/esp.4142).
- [7] H. Darmawan, T. R. Walter, K. S. Brotopuspito, and I. G. M. A. Nandaka, "Morphological and structural changes at the Merapi lava dome monitored in 2012–15 using unmanned aerial vehicles (UAVs)," *J. Volcanology Geothermal Res.*, vol. 349, pp. 256–267, Jan. 2018, doi: [10.1016/j.jvolgeores.2017.11.006](https://doi.org/10.1016/j.jvolgeores.2017.11.006).
- [8] H. Yang and G. Yao, "Hydropower development in Southwestern China," *IEEE Power Eng. Rev.*, vol. 22, no. 3, pp. 16–18, Mar. 2002, doi: [10.1109/mper.2002.989189](https://doi.org/10.1109/mper.2002.989189).
- [9] M. You and K. Hu, "Coordinated operation method of cascade hydropower stations considering runoff error," *J. Phys.: Conf. Ser.*, vol. 2195, no. 1, Feb. 2022, Art. no. 012016, doi: [10.1088/1742-6596/2195/1/012016](https://doi.org/10.1088/1742-6596/2195/1/012016).
- [10] M. F. K. Pasha et al., "Identifying high power-density stream reaches through refined geospatial resolution in hydropower resource assessment," *J. Water Resour. Plan. Manage.*, vol. 142, no. 2, Apr. 2016, Art. no. 06016001, doi: [10.1061/\(asce\)wr.1943-5452.0000599](https://doi.org/10.1061/(asce)wr.1943-5452.0000599).
- [11] H. Li, X. Li, Y. Ning, S. Jiang, and J. Zhou, "Dynamical process of the Hongshiyuan landslide induced by the 2014 Ludian earthquake and stability evaluation of the back scarp of the remnant slope," *Bull. Eng. Geol. Environ.*, vol. 78, pp. 2081–2092, Apr. 2019, doi: [10.1007/s10064-018-1233-6](https://doi.org/10.1007/s10064-018-1233-6).
- [12] N. Jiang et al., "Quantitative hazard assessment of rockfall and optimization strategy for protection systems of the Huashiya cliff, Southwest China," *Geomatics, Natural Hazards Risk*, vol. 11, no. 1, pp. 1939–1965, Sep. 2020, doi: [10.1080/19475705.2020.1819445](https://doi.org/10.1080/19475705.2020.1819445).
- [13] N. Jiang et al., "Quantitative hazard analysis and mitigation measures of rockfall in a high-frequency rockfall region," *Bull. Eng. Geol. Environ.*, vol. 80, no. 4, pp. 3439–3456, Apr. 2021, doi: [10.1007/s10064-021-02137-1](https://doi.org/10.1007/s10064-021-02137-1).
- [14] T. Lei et al., "The application of UAV remote sensing in mapping of damaged buildings after earthquakes," in *Proc. 10th Int. Conf. Digit. Image Process.*, 2018, vol. 10806, pp. 1408–1413, doi: [10.1117/12.2503163](https://doi.org/10.1117/12.2503163).
- [15] S. I. Jimenez-Jimenez, W. Ojeda-Bustamante, M. D. Marcial-Pablo, and J. Enciso, "Digital terrain models generated with low-cost UAV photogrammetry: Methodology and accuracy," *Int. Soc. Photogrammetry Remote Sens. Int. J. Geo-Inf.*, vol. 10, no. 5, May 2014, Art. no. 285, doi: [10.3390/ijgi10050285](https://doi.org/10.3390/ijgi10050285).
- [16] M. Jaboyedoff et al., "Use of terrestrial laser scanning for the characterization of retrogressive landslides in sensitive clay and rotational landslides in river banks," *Can. Geotech. J.*, vol. 46, no. 12, pp. 1379–1390, Dec. 2009, doi: [10.1139/t09-073](https://doi.org/10.1139/t09-073).
- [17] C. Fey and V. Wichmann, "Long-range terrestrial laser scanning for geomorphological change detection in alpine terrain-handling uncertainties," *Earth Surf. Processes Landforms*, vol. 42, pp. 789–802, Apr. 2017, doi: [10.1002/esp.4022](https://doi.org/10.1002/esp.4022).
- [18] A. Corsini, C. Castagnetti, E. Bertacchini, R. Rivola, F. Ronchetti, and A. Capra, "Integrating airborne and multi-temporal long-range terrestrial laser scanning with total station measurements for mapping and monitoring a compound slow moving rock slide," *Earth Surf. Processes Landforms*, vol. 38, pp. 1330–1338, Sep. 2013, doi: [10.1002/esp.3445](https://doi.org/10.1002/esp.3445).
- [19] R. Janoutova, L. Homolova, J. Novotny, B. Navratilova, M. Píkl, and Z. Malenovsky, "Detailed reconstruction of trees from terrestrial laser scans for remote sensing and radiative transfer modelling applications," *Silico Plants*, vol. 3, no. 2, Aug. 2021, Art. no. diab026, doi: [10.1093/insilicoplants/diab026](https://doi.org/10.1093/insilicoplants/diab026).
- [20] W. A. W. Aziz, M. Z. Syahmi, A. Anuar, and N. T. Khairul, "Terrain slope analyses between terrestrial laser scanner and airborne laser scanning," in *Proc. IEEE Control Syst. Graduate Res. Colloq.*, 2012, pp. 242–247, doi: [10.1109/icsgrc.2012.6287169](https://doi.org/10.1109/icsgrc.2012.6287169).
- [21] R. Pellicani et al., "UAV and airborne LiDAR data for interpreting kinematic evolution of landslide movements: The case study of the Montescaglioso landslide (Southern Italy)," *Geosciences*, vol. 9, no. 6, p. 248, Jun. 2019, doi: [10.3390/geosciences9060248](https://doi.org/10.3390/geosciences9060248).
- [22] M. R. James and S. Robson, "Mitigating systematic error in topographic models derived from UAV and ground-based image networks," *Earth Surf. Processes Landforms*, vol. 39, no. 10, pp. 1413–1420, Aug. 2014, doi: [10.1002/esp.3609](https://doi.org/10.1002/esp.3609).
- [23] M. R. James, S. Robson, S. d'Oleire-Oltmanns, and U. Nietham-Mer, "Optimising UAV topographic surveys processed with structure-from-motion: Ground control quality, quantity and bundle adjustment," *Geomorphology*, vol. 280, pp. 51–66, Mar. 2017, doi: [10.1016/j.geomorph.2016.11.021](https://doi.org/10.1016/j.geomorph.2016.11.021).
- [24] K. K. Singh and A. E. Frazier, "A meta-analysis and review of unmanned aircraft system (UAS) imagery for terrestrial applications," *Int. J. Remote Sens.*, vol. 39, no. 15/16, pp. 5078–5098, Aug. 2018, doi: [10.1080/01431161.2017.1420941](https://doi.org/10.1080/01431161.2017.1420941).
- [25] S. Valkaniotis, G. Papanthassiou, and A. Ganas, "Mapping an earthquake-induced landslide based on UAV imagery; case study of the 2015 Okeanos landslide, Lefkada, Greece," *Eng. Geol.*, vol. 245, pp. 141–152, Nov. 2018, doi: [10.1016/j.enggeo.2018.08.010](https://doi.org/10.1016/j.enggeo.2018.08.010).
- [26] E. De Beni, M. Cantarero, and A. Messina, "UAVs for volcano monitoring: A new approach applied on an active lava flow on Mt. Etna (Italy), during the 27 February–02 March 2017 eruption," *J. Volcanology Geothermal Res.*, vol. 369, pp. 250–262, Jan. 2019, doi: [10.1016/j.jvolgeores.2018.12.001](https://doi.org/10.1016/j.jvolgeores.2018.12.001).
- [27] M. V. Peppas et al., "Brief communication: Landslide motion from cross correlation of UAV-derived morphological attributes," *Natural Hazards Earth Syst. Sci.*, vol. 17, pp. 2143–2150, Dec. 2017, doi: [10.5194/nhess-17-2143-2017](https://doi.org/10.5194/nhess-17-2143-2017).
- [28] D. Turner, A. Lucieer, and S. M. de Jong, "Time series analysis of landslide dynamics using an unmanned aerial vehicle (UAV)," *Remote Sens.*, vol. 7, pp. 1736–1757, Feb. 2015, doi: [10.3390/rs70201736](https://doi.org/10.3390/rs70201736).
- [29] M. Jaboyedoff et al., "Use of LiDAR in landslide investigations: A review," *Natural Hazards*, vol. 61, pp. 5–28, Mar. 2012, doi: [10.1007/s11069-010-9634-2](https://doi.org/10.1007/s11069-010-9634-2).
- [30] G. Ventura et al., "Tracking and evolution of complex active landslides by multi-temporal airborne LiDAR data: The Montaguto landslide (Southern Italy)," *Remote Sens. Environ.*, vol. 115, pp. 3237–3248, Dec. 2011, doi: [10.1016/j.rse.2011.07.007](https://doi.org/10.1016/j.rse.2011.07.007).
- [31] A. Abellán et al., "Terrestrial laser scanning of rock slope instabilities," *Earth Surf. Processes Landforms*, vol. 39, pp. 80–97, Jan. 2014, doi: [10.1002/esp.3493](https://doi.org/10.1002/esp.3493).

- [32] A. Guerin et al., "Quantifying 40 years of rockfall activity in Yosemite valley with historical structure-from-motion photogrammetry and terrestrial laser scanning," *Geomorphology*, vol. 356, May 2020, Art. no. 107069, doi: [10.1016/j.geomorph.2020.107069](https://doi.org/10.1016/j.geomorph.2020.107069).
- [33] A. Kyriou, K. Nikolakopoulos, and I. Koukouvelas, "Timely and low-cost remote sensing practices for the assessment of landslide activity in the service of hazard management," *Remote Sens.*, vol. 14, Oct. 2022, Art. no. 4745, doi: [10.3390/rs14194745](https://doi.org/10.3390/rs14194745).
- [34] M. Barbarella, A. Di Benedetto, M. Fiani, D. Guida, and A. Lugli, "Use of DEMs derived from TLS and HRSI data for landslide feature recognition," *Int. Soc. Photogrammetry Remote Sens. Int. J. Geo-Inf.*, vol. 7, p. 160, Apr. 2018, doi: [10.3390/ijgi7040160](https://doi.org/10.3390/ijgi7040160).
- [35] Z. Xu, E. Xu, L. Wu, S. Liu, and Y. Mao, "Registration of terrestrial laser scanning surveys using terrain-invariant regions for measuring exploitative volumes over open-pit mines," *Remote Sens.*, vol. 11, no. 6, Mar. 2019, Art. no. 606, doi: [10.3390/rs11060606](https://doi.org/10.3390/rs11060606).
- [36] D. Zhou, K. Wu, R. Chen, and L. Li, "GPS/terrestrial 3D laser scanner combined monitoring technology for coal mining subsidence: A case study of a coal mining area in Hebei, China," *Natural Hazards*, vol. 70, no. 2, pp. 1197–1208, Jan. 2014, doi: [10.1007/s11069-013-0868-7](https://doi.org/10.1007/s11069-013-0868-7).
- [37] M. Barbarella and M. Fiani, "Monitoring of large landslides by terrestrial laser scanning techniques: Field data collection and processing," *Eur. J. Remote Sens.*, vol. 46, pp. 126–151, Jan. 2013, doi: [10.5721/EUJRS20134608](https://doi.org/10.5721/EUJRS20134608).
- [38] G. Bareth, J. Bendig, N. Tilly, D. Hoffmeister, H. Aasen, and A. Bolten, "A comparison of UAV- and TLS-derived plant height for crop monitoring: Using polygon grids for the analysis of crop surface models (CSMs)," *Photogrammetrie Fernerkundung Geoinf.*, no. 2, pp. 85–94, May 2016, doi: [10.1127/pfg/2016/0289](https://doi.org/10.1127/pfg/2016/0289).
- [39] M. Mukhlisin, H. W. Astuti, R. Kusumawardani, E. D. Wardihani, and B. Supriyo, "Rapid and low cost ground displacement mapping using UAV photogrammetry," *Phys. Chem. Earth*, vol. 130, Jun. 2023, Art. no. 103367, doi: [10.1016/j.pce.2023.103367](https://doi.org/10.1016/j.pce.2023.103367).
- [40] E. Puniach, W. Gruszczyński, P. Cwiąkała, and W. Matwij, "Application of UAV-based orthomosaics for determination of horizontal displacement caused by underground mining," *Int. Soc. Photogrammetry Remote Sens. J. Photogrammetry Remote Sens.*, vol. 174, pp. 282–303, Apr. 2021, doi: [10.1016/j.isprsjprs.2021.02.006](https://doi.org/10.1016/j.isprsjprs.2021.02.006).
- [41] H. Zhao et al., "The analyses for the experiments of high-resolution digital aero-photograph with UAV remote-sensing system," in *Proc. 15th Nat. Symp. Remote Sens. China - Remote Sens. Environ.*, 2006, vol. 6200, pp. 57–62, doi: [10.1117/12.681219](https://doi.org/10.1117/12.681219).
- [42] Y. Li, Z. Li, L. Tong, Y. Yan, and D. Guo, "A geometrical rectification algorithm of UAV remote sensing images based on flight attitude parameters," in *Proc. IEEE Int. Geosci. Remote Sens. Symp.*, 2011, pp. 487–490, doi: [10.1109/igarss.2011.6049171](https://doi.org/10.1109/igarss.2011.6049171).
- [43] N. Jiang et al., "A monitoring method integrating terrestrial laser scanning and unmanned aerial vehicles for different landslide deformation patterns," *IEEE J. Sel. Topics Appl. Earth Observ. Remote Sens.*, vol. 14, pp. 10242–10255, 2021, doi: [10.1109/jstars.2021.3117946](https://doi.org/10.1109/jstars.2021.3117946).
- [44] R. Lu and X. Yang, "Research on UAV large scale mapping and its elevation fitting," in *Proc. 3rd Int. Workshop Environ. Geosci.*, 2020, vol. 569, Art. no. 012078, doi: [10.1088/1755-1315/569/1/012078](https://doi.org/10.1088/1755-1315/569/1/012078).
- [45] L. Jianping, Y. Bisheng, C. Chi, and A. Habib, "NRLI-UAV: Non-rigid registration of sequential raw laser scans and images for low-cost UAV LiDAR point cloud quality improvement," *Int. Soc. Photogrammetry Remote Sens. J. Photogrammetry Remote Sens.*, vol. 158, pp. 123–145, Dec. 2019, doi: [10.1016/j.isprsjprs.2019.10.009](https://doi.org/10.1016/j.isprsjprs.2019.10.009).
- [46] S. Kim et al., "Continuous coastal monitoring using UAV photogrammetry," in *Proc. SPIE Conf. Earth Resour. Environ. Remote Sens.*, 2019, vol. 11156, pp. 327–332, doi: [10.1117/12.2533108](https://doi.org/10.1117/12.2533108).
- [47] C. Li, L. Shen, H. Wang, and T. Lei, "The research on unmanned aerial vehicle remote sensing and its applications," in *Proc. IEEE 2nd Int. Conf. Adv. Comput. Control*, 2010, pp. 644–647, doi: [10.1109/icacc.2010.5486720](https://doi.org/10.1109/icacc.2010.5486720).
- [48] H. Lin et al., "Structuring and applying micro-UAV remote sensing system for landslides monitoring," *J. China Three Gorges Univ.*, vol. 38, pp. 53–58, Oct. 2016, doi: [10.13393/j.cnki.issn.1672-948X.2016.05.010](https://doi.org/10.13393/j.cnki.issn.1672-948X.2016.05.010).
- [49] D. Lague, N. Brodu, and J. Leroux, "Accurate 3D comparison of complex topography with terrestrial laser scanner: Application to the Rangitikei canyon (N-Z)," *Int. Soc. Photogrammetry Remote Sens. J. Photogrammetry Remote Sens.*, vol. 82, pp. 10–26, Aug. 2013, doi: [10.1016/j.isprsjprs.2013.04.009](https://doi.org/10.1016/j.isprsjprs.2013.04.009).
- [50] Y. Feng, Q. Wang, and H. Zhang, "Total least-squares iterative closest point algorithm based on lie algebra," *Appl. Sci.-Basel*, vol. 9, no. 24, Dec. 2019, Art. no. 5352, doi: [10.3390/app9245352](https://doi.org/10.3390/app9245352).
- [51] Y. D. Rajendra et al., "Evaluation of partially overlapping 3D point cloud's registration by using ICP variant and cloud compare," in *Proc. ISPRS Tech. Commission VIII Symp.*, 2014, vol. 40–48, pp. 891–897, doi: [10.5194/isprsarchives-XL-8-891-2014](https://doi.org/10.5194/isprsarchives-XL-8-891-2014).
- [52] Z. Mao, S. Hu, N. Wang, and Y. Long, "Precision evaluation and fusion of topographic data based on UAVs and TLS surveys of a loess landslide," *Front. Earth Sci.*, vol. 9, Dec. 2021, Art. no. 801293, doi: [10.3389/feart.2021.801293](https://doi.org/10.3389/feart.2021.801293).
- [53] W. Zhang, Y. Chen, B. Yang, L. Zhang, C. Zhang, and X. Liu, "Experimental and numerical analyses on working performance of a high arch dam with deep-seated joints: YBT arch dam, China," *Arab. J. Geosci.*, vol. 12, no. 4, pp. 1–16, Feb. 2019, doi: [10.1007/s12517-019-4256-9](https://doi.org/10.1007/s12517-019-4256-9).
- [54] Y. Liu, W. Huang, G. Ma, S. Chen, and J. Wang, "Competitiveness of hydropower price and preferential policies for hydropower development in Tibet and the Sichuan-Yunnan Tibetan area of China," *Water Policy*, vol. 20, no. 6, pp. 1092–1111, Dec. 2018, doi: [10.2166/wp.2018.122](https://doi.org/10.2166/wp.2018.122).
- [55] K. Xu et al., "Estimation of degraded grassland aboveground biomass using machine learning methods from terrestrial laser scanning data," *Ecol. Indicators*, vol. 108, Jan. 2020, Art. no. 105747, doi: [10.1016/j.ecolind.2019.105747](https://doi.org/10.1016/j.ecolind.2019.105747).
- [56] F. Wang, C. Xu, Z. Li, M. Anjum, and L. Wang, "Applicability of an ultra-long-range terrestrial laser scanner to monitor the mass balance of Muz Taw Glacier, Sawir Mountains, China," *Sci. Cold Arid Regions*, vol. 10, no. 1, pp. 47–54, Feb. 2018, doi: [10.3724/sp.j.1226.2018.00047](https://doi.org/10.3724/sp.j.1226.2018.00047).
- [57] K. Julge et al., "Combining airborne and terrestrial laser scanning to monitor coastal processes," in *Proc. IEEE/OES Baltic Int. Symp.*, Jan. 2023, vol. 14, no. 1, pp. 1–10, doi: [10.1109/baltic.2014.6887874](https://doi.org/10.1109/baltic.2014.6887874).
- [58] A. Kyriou, K. Nikolakopoulos, and I. Koukouvelas, "Synergistic use of UAV and TLS data for precise rockfall monitoring over a hanging monastery," in *Proc. Conf. Earth Resour. Environ. Remote Sens.*, 2022, vol. 12268, pp. 34–45, doi: [10.1117/12.2636150](https://doi.org/10.1117/12.2636150).



Xiang-Long Luo received the B.S. degree in water resource and hydropower engineering in 2022 from Sichuan University, Sichuan, China, where he is currently working toward the master's degree in artificial intelligence applications.

His research interests include landslide monitoring and remote sensing technologies.



Nan Jiang received the B.S. degree in water resource and hydropower engineering in 2015, and the M.S. degree in hydraulic structural engineering in 2021 from Sichuan University, Sichuan, China, where he is currently working toward the Ph.D. degree in hydraulic structural engineering.

He was an Engineer with Sichuan University Engineering Design and Research Institute for two years after receiving the B.S. degree. His main research interests include remote sensing technologies and their application in the identification and mitigation of natural hazards, such as landslides and rockfalls.



Hai-Bo Li received the B.S. degree in water resource and hydropower engineering, the M.S. degree in hydraulic structural engineering, and the Ph.D. degree in hydraulic structural engineering from Sichuan University, Sichuan, China, in 2015, 2017, and 2020, respectively.

He works as a distinguished Research Fellow with Sichuan University after receiving the Ph.D. degree. His main research interests include the integrated research and development of multisource noncontact monitoring technologies, such as 3-D laser scanning,

ground-based synthetic aperture radar and UAVs, and their application in engineering safety and geological disaster monitoring and early warning.



Huai-Xian Xiao received the B.S. degree in water resource and hydropower engineering in 2021 from Sichuan University, Sichuan, China, where he is currently working toward the master's degree in artificial intelligence applications.

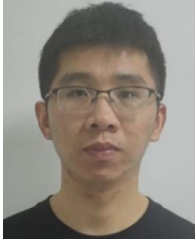
His research interests include image processing and computer vision, especially their application in the field of geological disaster monitoring.



Jia-Wen Zhou received the M.S. and Ph.D. degrees in geotechnical engineering from Hohai University, Nanjing, China, in 2005 and 2008, respectively.

He is a Professor with the College of Water Resources and Hydropower, Sichuan University, Sichuan, China. He leads the Engineering Technology and Disaster Prevention Team of Sichuan University. His research mainly focuses on the monitoring, risk assessment, early warning, and emergency management of geologic hazards.

Dr. Zhou is an editorial board member of international journals such as the *Bulletin of Engineering Geology and the Environment* and *Journal of Mountain Science*.



Xing-Zhen Chen received the B.S. degree in water resource and hydropower engineering in 2019 from Shandong Agricultural University, Shandong, China, where he is currently working toward the master's degree in artificial intelligence applications.

His research interests include artificial intelligence applications related to landslide disasters.